Statistical perspective on embrittling potency for intergranular fracture

M. E. Fernandez,[1] R. Dingreville,[2] and D. E. Spearot[1,*]

[1]*Department of Mechanical and Aerospace Engineering, University of Florida, Gainesville, Florida 32611, USA*

[2]*Center of Integrated Nanotechnologies, Sandia National Laboratories, Albuquerque, New Mexico 87123, USA*

(Received 8 February 2022; accepted 27 July 2022; published 15 August 2022)

Embrittling potency is a thermodynamic metric that assesses the influence of solute segregation to a grain boundary (GB) on intergranular fracture. Historically, authors of studies have reported embrittling potency as a single scalar value, assuming a single segregation site of importance at a GB and a particular cleavage plane. However, the topography of intergranular fracture surfaces is not generally known *a priori*. Accordingly, in this paper, we present a statistical ensemble approach to compute embrittling potency, where many free surface (FS) permutations are systematically considered to model fracture of a GB. The result is a statistical description of the thermodynamics of GB embrittlement. As a specific example, embrittling potency distributions are presented for Cr segregation to sites at two Ni ⟨111⟩ symmetric tilt GBs using atomistic simulations. We show that the average embrittling potency for a particular GB site, considering an ensemble of FS permutations, is not equal to the embrittling potency computed using the lowest energy pair of FSs. A mean GB embrittlement is proposed, considering both the likelihood of formation of a particular FS and the probability of solute occupancy at each GB site, to compare the relative embrittling behavior of two distinct GBs.

DOI: 10.1103/PhysRevMaterials.6.083602

I. INTRODUCTION

Atomic solutes in metals are prone to segregation where, depending on energetic favorability, they may migrate toward grain boundaries (GBs) [1] or other regions of free volume [2,3]. Solute segregation can be intended and beneficial, such as in the case of grain size stabilization in nanocrystalline metals [4–6], or it can have deleterious effects on material properties, such as in the case of hydrogen embrittlement [7,8]. A variety of material property changes result from segregation [2,9,10], but we focus specifically on GB embrittlement in this paper, where solute segregation changes the work of GB separation. GBs are known to be energetically favorable pathways for fracture [11,12]; thus, embrittlement caused by solute segregation can have a profound impact on the strength and ductility of an alloy [13].

McLean [14] provided a thermodynamic description of GB solute segregation in binary systems by defining an isotherm that relates the concentration of solutes segregated to a GB to bulk concentration and a solute segregation energy. The McLean [14] isotherm assumed that segregation energies to each GB site were equal. However, different atomic sites at a GB have different geometric and chemical configurations. White and Stein [15] and White and Coghlan [16] showed evidence that solutes do not segregate to all GB sites equally and defined a different isotherm to account for site-specific segregation energetics. Building upon GB segregation energy, the thermodynamic concept of embrittling potency was proposed by Rice and Wang [13]. Embrittling potency for a GB was defined as the difference in energy between solute segregation to the GB and solute segregation to a corresponding free surface (FS). Furthermore, Rice and Wang [13] argued that embrittlement was related to the reduction of the work of separation of a GB due to the presence of the segregant. The amount by which the ideal work of separation was changed by solute segregation could be written as $\Delta E_b \Gamma$, where ΔE_b is the embrittling potency, and Γ is the number of segregants per unit area on the interface (coverage). Hence, embrittling potency served as a scalar measure of the impact of a solute on GB fracture. Several authors have since studied site-specific embrittling potency for various metals [7,17–22]. For example, Razumovskiy *et al.* [20,22] studied embrittlement in a variety of Ni-based alloys using first-principles methods. These authors used their findings on GB embrittling potency to tailor compositions for Ni-based superalloys with higher mechanical strength. Recently, Aksoy *et al.* [21] introduced a method for comparing embrittling potencies between different symmetric tilt GBs (STGBs) embedded within a theoretical polycrystal. By defining a statistical method of analysis which calculates GB site occupancy within a polycrystalline environment and performing atomistic simulations of solute segregation to STGBs and their corresponding FSs, Aksoy *et al.* [21] identified critical GBs with outstanding embrittling behavior in the case of S segregation in a Ni polycrystal.

In previous works that focused on embrittling potencies, a prevalent underlying assumption was made that GB fracture occurred on a predetermined, flat cleavage plane [7,13,17–21,23]. The consequence of this assumption is that a single value of the embrittling potency was computed for each atomic site. However, GB fracture can be tortuous, producing atomically rough surfaces depending on the boundary and loading conditions [18,23–26]. For example, tensile tests of H-embrittled Inconel from Seita *et al.* [25] showed tortuous

*dspearot@ufl.edu

intergranular fracture surfaces resulting from a mixture of brittle and ductile fracture. Atomistic simulations from Yamakov *et al.* [26] showed that unstable crack propagation in intergranular fracture can result in microvoid coalescence producing a variety of nonminimum energy surface topographies. Molecular dynamics simulations from the work of Spearot *et al.* [24] and Bitzek *et al.* [27] clearly demonstrated jagged cleavage planes with surface roughness between 3 and 6 Å normal to the GB. Such observations imply that a FS pair can form that does not correspond to the static minimum energy FSs for that lattice orientation. Unfortunately, the influence of intergranular fracture surface topography on embrittling potency has not been discussed or evaluated at length, although one recent study of H embrittlement used a small set of atomically flat FSs [28].

In this paper, we examine embrittling potency of solutes at GBs from a thermodynamic and statistical perspective. Our approach considers an ensemble of possible FS topographies resulting from an implied tortuous intergranular crack propagation. We illustrate this approach via calculations of Cr segregation to individual GB sites in Ni. Ni-Cr is chosen as a model alloy system since the atomic mismatch between Ni and Cr is negligible, limiting the effects of compositional expansion and the associated elastic release of stresses around the segregating solute [29]. Additionally, the origin of segregation in this alloy system is well documented in previous studies [20,22,29,30], making it an ideal candidate for this paper. Atomistic calculations of segregation across the ensemble of FSs produce a distribution of embrittling potencies for each GB site, showing that some GB sites exhibit strengthening or embrittling behavior depending on the FS topography. Analyzing the new ensemble data requires a different set of tools; thus, we propose an ensemble average of the embrittling potencies that accounts for the probability density associated with FS formation, based on calculations of equilibrated FS energies. Additionally, we propose a mean GB embrittlement which considers the ensemble average embrittling potencies, the probability of site occupancy by a solute, and the area of the GB unit cell. The mean GB embrittlement condenses the embrittling potency distributions into a single scalar value representative of the full ensemble that can be used to compare two different GBs when the embrittling potency distributions are themselves unique.

Note, in this paper, we do not consider the dynamics of crack propagation along a GB. Rather, we present a thermodynamic and statistical perspective on the calculation of embrittling potency. We assume fracture conditions where solutes do not move from their site position between GB and FS models, although local relaxations are allowed via energy minimization within the framework of molecular statics calculations. Thus, the results described below are best applied to cases of crack initiation.

II. METHODS

A. Material selection, embedded-atom method potential, and software

The selected material system consists of bulk Ni as the solvent with Cr solutes. We choose this system since there is <5% difference between the atomic radii of Ni and Cr. Thus, embrittlement can be attributed to chemistry only since Cr substitution will not create significant mechanical strain in the lattice for the solvent-solute pair. Additionally, the segregation behavior of Cr in Ni has been well documented by Startt *et al.* [29,30] using *ab initio* calculations, providing a point of validation for the results of our calculations. We use the LAMMPS molecular dynamics software [31,32] with an embedded-atom method (EAM) potential designed by Zhou *et al.* [33]. While originally designed as an Fe-Ni-Cr potential, this potential was fitted to accurately simulate the formation of different material phases and provide stacking-fault energies which aligned with experimental results. Stacking-fault energies and material phase emulation are essential in the modeling of GBs and segregation. While other potentials were also considered for study [34,35], the Zhou *et al.* [33] potential was chosen as the best option. The mean and breadth of the distributions that are presented in Sec. III are likely to be sensitive to the interatomic potential; however, the fundamental concepts of the existence of an embrittling potency distribution for each GB site and the proposed ensemble average are valid regardless of the choice of interatomic potential.

We use OVITO [36] to visualize the resulting structures and identify specific atoms at and surrounding the GBs for segregation and embrittlement analysis. Within a unit cell area on the GB plane, we identify and number unique atom sites based on centrosymmetry [37].

B. GB models

We select a pair of complementary STGBs with a [111] misorientation axis for analysis: the $\Sigma 7$ {213} and $\Sigma 21$ {415} STGBs. These GBs are chosen because the adjoining lattice regions exhibit similar characteristics [38]. To construct the STGBs, we create two regions, top and bottom, in a simulation cell with periodic boundary conditions in all three cartesian directions, as shown in Fig. 1(a). The misorientation axis $M = [111]$ is defined along the x axis, parallel to the GB plane, while the normal to the GB plane N in the top lattice region is defined as $[\bar{4}15]$ for the $\Sigma 21$ STGB and $[\bar{2}13]$ for the $\Sigma 7$ STGB. We populate both regions with Ni atoms in a face-centered cubic crystal structure oriented according to those crystallographic directions.

The dimensions of the top and bottom regions must be integer multiples of the repeating distance of the lattice determined from the crystallographic orientation to satisfy periodic boundary conditions. In this paper, we choose repeating distances to be $8 \times 7 \times 6$ units in the x, y, and z directions, respectively. Hence, the $\Sigma 21$ {415} model has the dimensions $48.7 \times 66.2 \times 91.8$ Å, and the $\Sigma 7$ {213} model has the dimensions $48.7 \times 114.7 \times 53.0$ Å. These dimensions are significantly larger than the cutoff distance for the EAM potential used in this paper; thus, they are sufficient for convergence of atomistic calculations of segregation energies.

To find the minimum energy configuration of each GB, we perform a γ-surface construction. Within this construct, we translate the top lattice region in the x, y, and z directions relative to the bottom lattice region, with a conjugate gradient molecular statics (energy minimization) calculation performed after each translation. The total translation distance

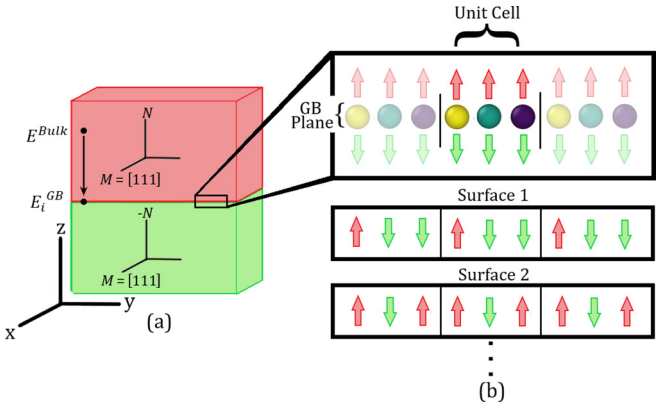

FIG. 1. (a) Lattice orientations for both top (red) and bottom (green) regions illustrating the grain boundary (GB) construction. Cr is substituted into a GB site, and energy minimization is performed to obtain E_i^{GB}. Then Cr is swapped from the GB into the bulk, and energy minimization is performed to obtain E^{Bulk}. (b) Example of the free surface topography permutation process with a fictitious GB with three atoms at the GB plane in one repeating unit cell. Decisions for an atom to move up or down during fracture are made within a single GB unit cell, and then those decisions are repeated in all other repeating units.

in the x and y directions is equal to the repeating distance, while the translation distance in the z direction is 2 Å, roughly the width of a layer of atoms in the z direction. Since the z translation may cause atoms to overlap each other, atoms from the bottom region are deleted if they are within 1 Å of atoms in the top region. Here, 20 increments in the x and y directions and 10 increments in the z direction provide 4000 initial configurations for determination of the lowest energy GB structure.

C. FS models

We initially assume that fracture occurs along the GB plane, as illustrated in Fig. 1(b). Atoms along the GB plane in a single unit cell are partitioned into either the top or bottom region, and the partitions are repeated periodically for each unit cell on the GB plane. For example, referring to the fictitious GB in Fig. 1(b), the ensemble contains a permutation ($j = 2$) where a pair of unrelaxed FSs is formed by moving atoms within a unit cell in an up-down-down pattern. The top and bottom regions are then separated by 20 Å, and conjugate gradient molecular statics are used to determine the relaxed FS topography. Energy minimization is performed with no external pressure. Generating all permutations with this method results in 32 (2^5) FS permutations for the {415} GB and 512 (2^9) for the {213} GB. We call this set of fracture permutations the *periodic GB ensemble*. Note this procedure implicitly assumes that solute concentration does not change at the GB during fracture and that the solute does not move significantly from its site location, although it may relax locally during energy minimization.

Note this method produces FSs in pairs for STGBs. For each FS where an atom site is partitioned into the top group, there exists a complementary FS where the opposite is true. Each FS should have the same free energy and segregation energy as its mirror duplicate; thus, we keep data resulting from these duplicate surfaces to verify the consistency of the simulation results.

Of course, each GB could have more possible FS permutations than those in the periodic GB fracture ensemble. To limit the total number of molecular statics calculations that are necessary for every site in the GB, we initially assume that fracture occurs along the GB plane and that decisions are periodic for all GB unit cells. We hypothesize that the ensemble resulting from these decisions is representative of the ensemble of all possible FSs. To test this hypothesis, in Sec. III B, we include some atoms from one atomic layer above the GB plane in the FS permutation process to understand how this expanded set changes the distribution of FS energy. We call this set of permutations the *periodic expanded ensemble*.

In addition, to verify how FS topography neighboring the analyzed GB unit cell can affect segregation and embrittlement, we create a third set of fracture permutations. In this new set, a single GB unit cell is permuted in the same way as the periodic GB ensemble; however, periodicity is not enforced across the entire GB plane. Instead, the remainder of the GB adopts an atomically flat fracture topography. Hence, we call this ensemble the *flat neighboring ensemble*. For the Σ7 {213} STGB, since the GB cell is composed of three identical units, we include translations of the flat fracture region in the y direction, shifting the starting location of the permuted region. Ultimately, for both STGBs, the average embrittling potency is compared against the periodic GB ensemble.

D. Segregation energy and embrittling potency

The segregation energy of a solute to a GB or FS, $\Delta E_{\mathrm{seg},i}^{\mathrm{GB/FS}}$, is defined as the difference between the energy of a system with a solute atom at a substitutional site at the GB or FS, $E_i^{\mathrm{GB/FS}}$, and the energy of a system with a solute atom at a substitutional site within the bulk E^{Bulk} [16]:

$$\Delta E_{\mathrm{seg},i}^{\mathrm{GB/FS}} = E_i^{\mathrm{GB/FS}} - E^{\mathrm{Bulk}}. \tag{1}$$

Here, i denotes the site type. Negative segregation energy implies that solute segregation to the GB or FS is energetically preferred.

Figure 1 illustrates how these values are acquired. We initially substitute a Cr atom into the desired Ni GB site location. Following an energy minimization, we compute the potential energy of the system as E_i^{GB}. Then we swap the GB site Cr with a Ni atom from within the bulk and perform another energy minimization to calculate E^{Bulk}.

For calculation of $\Delta E_{\mathrm{seg},i}^{\mathrm{FS}}$, we must include an additional step. As before, we substitute a Cr atom into the desired surface site and perform an energy minimization to calculate E_i^{FS}. Then we swap the surface Cr with a Ni atom within the bulk. Unlike before, we restrict the relaxation of all atoms except for those within a sphere around the bulk Cr of radius equal to the interatomic cutoff distance of 5.7 Å. Then we calculate the energy again as E^{Bulk}. The purpose of ordering the substitutions and locally minimizing the bulk Cr is to limit model-scale reconstruction of the FS during energy minimization. If the FS reconstructs, then the FS permutation of interest would not be the same as the FS that results from the energy minimization.

This would lead to inconsistencies in the calculation of the embrittling potency. Ultimately, the surfaces for which we prevent reconstruction have much higher FS energies than the minimum energy FSs (difference >200 mJ/m^2) and thus will end up being weighted lower when averages are performed in Sec. IV, so local minimization should not notably impact the results of this paper.

Once we have segregation energies for the GB and each FS, embrittling potency can be calculated. The embrittling potency of a particular GB site $\Delta E_{b,i}$ is defined using the Rice-Wang formulation [13]:

$$\Delta E_{b,i} = \Delta E^{\mathrm{GB}}_{\mathrm{seg},i} - \Delta E^{\mathrm{FS}}_{\mathrm{seg},i}. \tag{2}$$

A positive $\Delta E_{b,i}$ denotes embrittling, whereas a negative $\Delta E_{b,i}$ denotes strengthening. Note that Eq. (1) computes a single value of $\Delta E^{\mathrm{GB}}_{\mathrm{seg},i}$ for each GB site, but each GB site exists on many possible sampled FSs (Fig. 1), providing a distribution of values for $\Delta E^{\mathrm{FS}}_{\mathrm{seg},i}$. Hence, each GB site will have a distribution of embrittling potencies $\Delta E_{b,i}$ computed via Eq. (2).

III. RESULTS

The objective of this paper is to show how distributions of embrittling potencies computed using different FS topographies can contribute to an ensemble average and hence a more complete understanding of solute embrittlement. To do so, we must gather the following information: solute segregation energies to the GBs (Sec. III A), embrittling potencies for each FS permutation for the STGBs (Sec. III B), and relaxed FS energies, which will define weighting in the ensemble average (Sec. III C). Note for completeness, we present embrittling potency distributions for all Ni GB sites, even if they are antisegregation sites that would never be occupied by the Cr solute. In the ensemble average (Sec. IV), we employ the McLean isotherm [14–16] which effectively addresses the coupling between GB site occupancy and embrittlement.

A. GB segregation energies

Figure 2(a) shows the minimum energy $\Sigma7$ {213} and $\Sigma21$ {415} STGB structures. GB structural units are labeled according to the nomenclature presented by Wang *et al.* [39]. Figure 2(b) shows maps of segregation energies for a Cr solute to sites within these STGBs. The most energetically favorable segregation sites at the GB plane are sites 2, 5, and 8 for the $\Sigma7$ {213} boundary and site 2 for the $\Sigma21$ {415}. Interestingly, these sites are associated with the F structural units in the case of the $\Sigma7$ {213} STGB, while they are associated with the E structural unit in the $\Sigma21$ {415} STGB. On the other hand, the largest antisegregation sites are sites 1, 4, and 7 for the $\Sigma7$ {213} STGB and site 4 for the $\Sigma21$ {415} STGB. In both GBs, these antisegregation sites are associated with the F structural unit and are positioned near pockets of free volume within the GB structure.

The solute segregation energy map for the $\Sigma7$ {213} STGB illustrates a pattern of energies that repeats in unison with the structural unit description, which is expected. The regular geometric pattern ensures that each FE structural unit block is identical to its neighbor, resulting in the triplet data shown in Fig. 2(b) for the $\Sigma7$ {213} STGB.

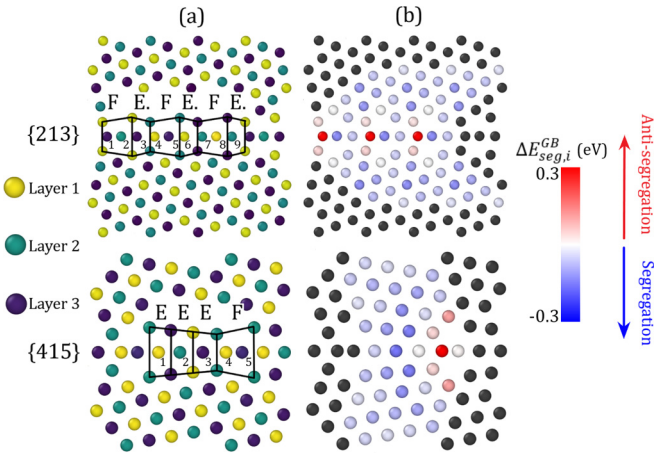

FIG. 2. (a) Minimum energy structure of the $\Sigma7$ {213} and $\Sigma21$ {415} symmetric tilt grain boundaries (STGBs) in Ni. Grain boundary (GB) sites are numbered for reference and colored by {111} atomic layer to identify structural units. The structural unit nomenclature was developed by Wang *et al.* [39]. (b) Map of Cr solute segregation energies for $\Sigma7$ {213} and $\Sigma21$ {415} STGBs. Units are in electronvolts. Negative values indicate favorable solute segregation, while positive values indicate antisegregation. Gray atom sites are not evaluated.

Segregation energies provide sufficient information to determine equilibrium concentrations at the GB. According to the site-specific interpretation of the McLean isotherm [16], the atomic percent of sites i occupied by solutes X^{GB}_i can be determined via

$$X^{\mathrm{GB}}_i = \frac{X^{\mathrm{Bulk}} \exp\left(-\frac{\Delta E^{\mathrm{GB}}_{\mathrm{seg},i}}{k_{\mathrm{B}}T}\right)}{1 - X^{\mathrm{Bulk}} + X^{\mathrm{Bulk}} \exp\left(-\frac{\Delta E^{\mathrm{GB}}_{\mathrm{seg},i}}{k_{\mathrm{B}}T}\right)}, \tag{3}$$

where X^{Bulk} is the atomic percent of solutes in the bulk lattice, k_{B} is the Boltzmann constant, and T is the absolute temperature, taken to be $T = 300$ K in this paper to emulate room temperature conditions. We broadly use the term *site occupancy* when describing solute occupation of sites at the GB. Site occupancy is often taken to mean either "the probability that a site i is occupied by a solute" or "the atomic percent of sites i occupied by a solute". We use these contexts interchangeably throughout this paper.

The choice of X^{Bulk} should be small, as the atomistic simulations in this paper are in a dilute limit where solute-solute interactions are not considered. Wagih and Schuh [40] reported that the limit for dilute studies lies at $X^{\mathrm{Bulk}} \cong 0.02$ or 2% for Mg segregation in Al. Beyond this limit, real dilute segregation behaviors diverge from the nondilute approximations due to solute-solute interactions. Al-Mg is not identical to Ni-Cr; however, the interatomic potential for Al-Mg [41] used by Wagih and Schuh [40] has a similar cutoff distance to the Ni-Cr potential used in this paper, and they both show energetic preference for solvent-solvent interactions over solute-solute interactions. Hence, it is reasonable to assume that the underlying cause of nondilute behavior,

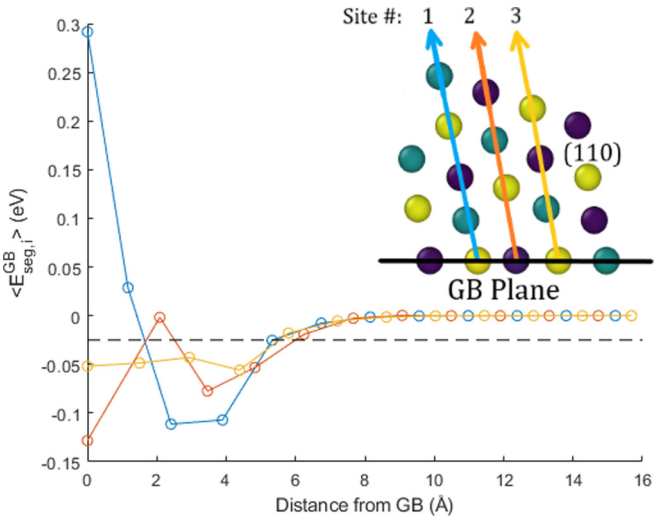

FIG. 3. Segregation energy vs distance from the grain boundary (GB) plane along ⟨110⟩ directions for the Σ7 {213} symmetric tilt GB (STGB). The cutoff criterion is indicated above the dashed black line. Atoms in the figure inlay are colored by different {111} planes, as shown in Fig. 2(a).

solute-solute interaction, is similar for both cases, and we take $X^{\text{Bulk}} = 2\%$ for our calculations. Note there is nothing that precludes the extension of our method to the nondilute case, but that is beyond the scope of this paper.

Frequently, studies which discuss GB width look toward geometric indicators such as centrosymmetry or common neighbor analysis (CNA) to determine which sites are part of the GB and which sites belong in the bulk [42,43]. However, our method is not concerned with structural unit geometry but instead with the thermodynamic impact of a segregant on GB fracture. Hence, we define GB width through a segregation energy cutoff for the purpose of studying embrittlement. Atoms along ⟨110⟩ crystallographic directions outward from the GB plane are included in the analysis until the segregation energy diminishes to a value between −0.025 and 0.0 eV since sites with segregation energy within this range will have $X_i^{\text{GB}} < 5$ at. % [computed using Eq. (3)], which we consider to be negligible. Figure 3 demonstrates for the three unique Σ7 {213} STGB sites how we implement this criterion along ⟨110⟩ crystallographic paths. Based on the data, this criterion provides a GB width of ∼6 Å on either side of the GB plane. An identical criterion is appropriate for determining GB sites for the Σ21 {415} STGB.

Note this GB width criterion still includes some sites with positive segregation energy within the GB, which would have $X_i^{\text{GB}} \cong 0$. This includes sites 1, 4, and 7 in the Σ7 {213} STGB and site 4 in the Σ21 {415} STGB. For completeness, we include these sites in the embrittling potency calculations; however, they will not impact the GB work of separation since they will never be occupied by solute. In Sec. IV, we address this by weighting GB site embrittling potencies by GB site occupancy.

B. Embrittling potency distributions

Segregation energy and embrittling potency calculations are performed for all GB sites identified in Fig. 2(b); however, in this section, we limit our demonstration of embrittling potency distributions to the numbered atoms at the GB plane because these atoms contain the extrema of GB segregation energies. Figures 4(a) and 4(b) show embrittling potency distributions for GB sites at the Σ7 {213} and Σ21 {415} STGBs, respectively. The box-whisker plots show condensed distributions of embrittling potencies for each site type. The red line denotes the mean, the box denotes the interquartile range, and the whiskers denote the data beyond the third quartile and before the first quartile. Red crosses denote statistical outliers.

Each box-and-whisker corresponds to a histogram which expands the distribution in detail. Examples of these histograms are shown in Fig. 4(a) for site 9 in the Σ7 {213} STGB and in Fig. 4(b) for site 5 in the Σ21 {415} STGB. Each histogram is fit with a skew-normal distribution:

$$F(\Delta E_{b,i}) = \frac{2}{\sigma}\frac{1}{\sqrt{2\pi}}\exp\left[-\frac{\left(\frac{\Delta E_{b,i}-\mu}{\sigma}\right)^2}{2}\right] \times \left\{\frac{1}{2}\left[1+\text{erf}\left(\lambda\frac{\Delta E_{b,i}-\mu}{\sigma\sqrt{2}}\right)\right]\right\} \quad (4)$$

where λ, μ, and σ are the skew, location, and shape of the distribution, respectively. The use of this distribution model to fit these results is inspired by the work of Wagih and Schuh [44], for which they show how closely a well-fit skew-normal distribution can approximate the density of states based on segregation energy. Skew-normal distributions are flexible distributions capable of capturing a variety of behaviors which have nearly normal behavior, so this function is equally applicable here.

Each box-and-whisker in Fig. 4 contains a black dot indicating the embrittling potency for the indicated site associated with the minimum energy FSs. Regardless of the segregation site and GB considered, the value of embrittling potency associated with the minimum energy FSs does not lie at the mean of observations nor at the extrema but rather at an arbitrary value within the distribution. Hence, the use of the minimum energy FS does not necessarily correlate to high, low, or even average embrittling potency when an ensemble of FSs is considered.

Figure 4 shows that GB sites can be embrittling or strengthening in nature depending on the intergranular fracture surface topography. Recall, the most energetically favorable sites for Cr segregations are 2, 5, and 8 for the Σ7 {213} STGB and site 2 for the Σ21 {415} STGB. Each of these sites shows a spectrum of behavior depending on the topography of the FS. For example, for the Σ7 {213} STGB, sites 2, 5, and 8 show a mean positive embrittling potency (embrittling). However, many of the sampled FSs display a negative embrittling potency (strengthening) for these sites. Similarly, for the Σ21 {415} STGB, site 2 shows a mean strengthening behavior; however, the box-whisker plot indicates that ∼25% of the sampled FSs show embrittling behavior. For all sites along the GB, the tails of the embrittling potency distributions show both embrittling and strengthening behavior. Studying a single FS may capture either the embrittling or strengthening behavior but would ignore the spectrum of possible embrittling potencies resulting from the ensemble of possible FSs.

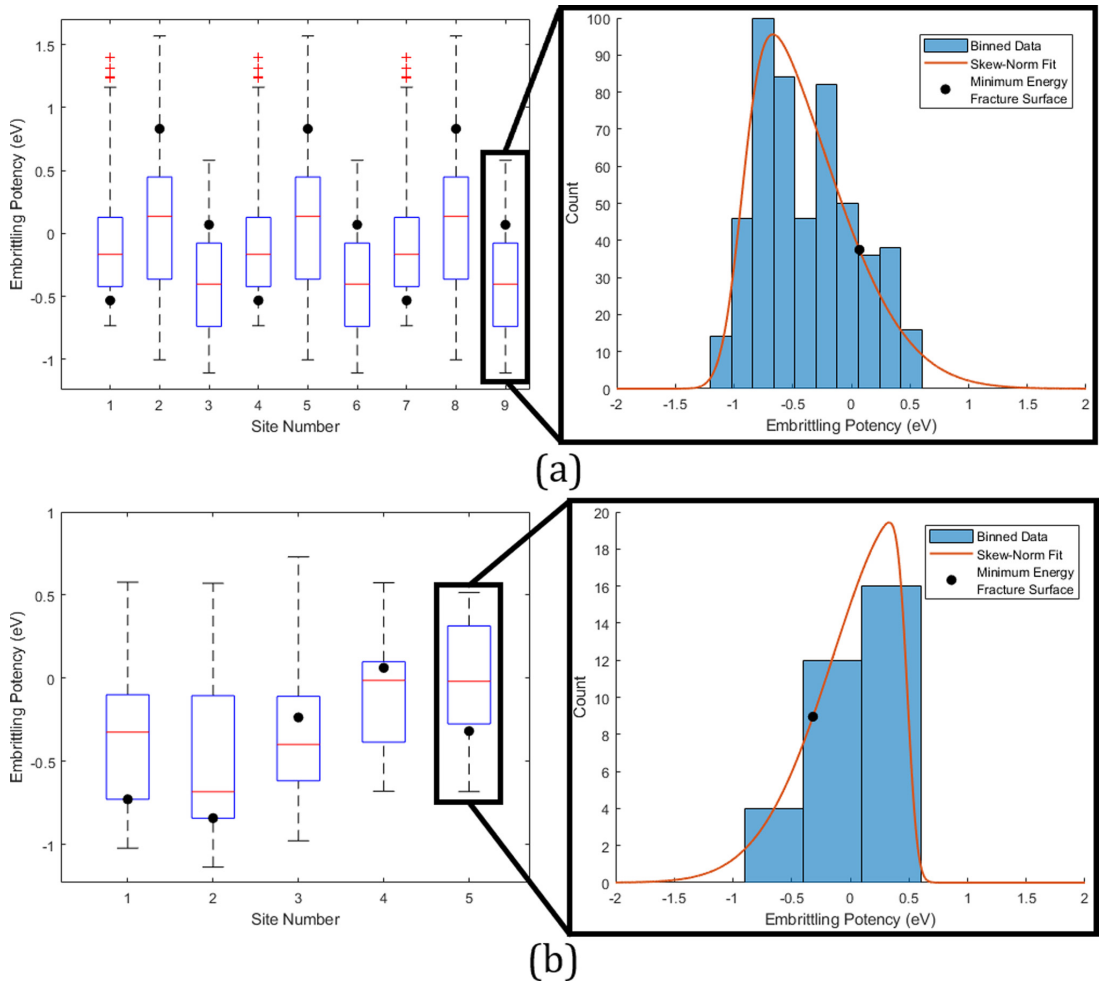

FIG. 4. Distributions of embrittling potencies for (a) Σ7 {213} symmetric tilt grain boundary (STGB) sites with a detailed histogram for site 9 and (b) Σ21 {415} STGB sites with a detailed histogram for site 5. Distributions are represented compactly as box-and-whisker plots, with plus symbols denoting statistical outliers. The dots indicate embrittling potencies associated with the relaxed minimum energy free surfaces.

These distributions elucidate the embrittling nature of a particular GB site for a selection of intergranular crack surface topographies, but they are not useful in this form for comparing segregation-induced embrittlement between two GBs. Previously, Aksoy *et al.* [21] used a combination of site occupancy probability and embrittling potency to make meaningful comparisons between GBs. However, to meaningfully make conclusions about relative embrittlement of two GBs when considering an ensemble of FSs, we must develop new tools which include the likelihood of FS formation the probability of segregation to a particular GB site.

C. FS energies

Figures 5(a) and 5(b) show relaxed FS energies for all FS permutations used to compute embrittling potency distributions for the Σ7 {213} and Σ21 {415} STGBs. These histograms demonstrate the wide variety of surface permutations tested in the generation of embrittling potency data. We uniquely determine the bin width of these histograms via the Freedman-Diaconis rule, which uses the interquartile range [45]. Since the pair of FSs generated are asymmetric with respect to the cleavage plane, the FS energies plotted are the average energies for both FSs.

For each GB, one pair of FSs stands out as the minimum energy surface topography. These minimum energy surfaces occur when all atoms at the GB plane are assigned to either the top or bottom lattice during fracture. Hence, the minimum energy FS does not split the GB plane as assumed in the works of Razumovskiy *et al.* [20] and Aksoy *et al.* [21] but rather delaminates the GB plane from the adjacent plane of atoms cleanly.

To show that our method of systematically generating FSs produces a representative ensemble of FSs, using the Σ7 {213} STGB as an example, we include FS energies from the periodic expanded ensemble. This increases the number of FS permutations from 512 to 4096 (2^{12}), each of which would need to be evaluated to compute segregation for all GB sites. However, the addition of these new surfaces does not expand the range of relaxed FS energies, as shown in Fig. 5(c); thus, FSs created using GB sites only are representative of the probable range of FS energies for these GBs.

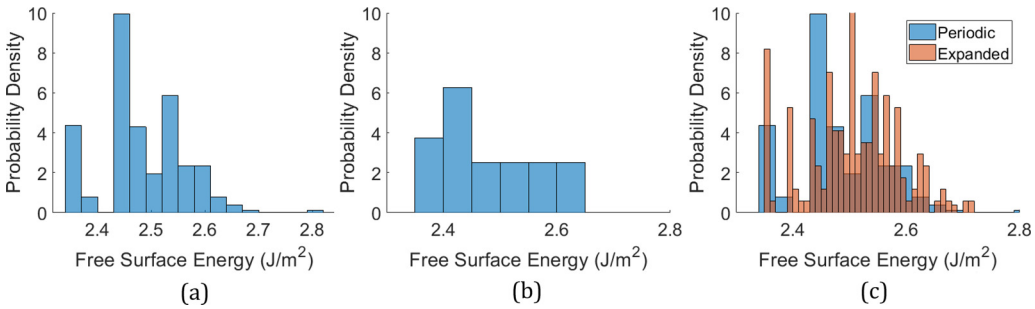

FIG. 5. Histograms showing relaxed free surface (FS) energies for FS topographies of the (a) Σ7 {213} and (b) Σ21 {415} symmetric tilt grain boundaries (STGBs). The distributions generally skew left toward lower FS energies. (c) Overlayed histograms of FS energies for fracture of the Σ7 {213} STGB. The periodic histogram includes the periodic grain boundary (GB) ensemble shown in Fig. 3(a), while the expanded histogram shows the periodic expanded ensemble that includes the GB plane atomic sites, as well as three atomic sites from the adjacent atomic plane above it. Note that the ranges of the FS energies are very similar.

IV. ENSEMBLE AVERAGING

To utilize the data computed from different FS permutations, we present a method for condensing the tens of thousands of embrittling potencies computed in Sec. III into metrics that can be related back to fundamental concepts presented by Rice and Wang [13]. A graphical overview of this approach is shown in Fig. 6. First, we average the embrittling potencies over the ensemble of FSs j for each GB site i, $\Delta E_{b,ij}$, to get ensemble averaged values for each site $\langle \Delta E_{b,i} \rangle$. Then an occupancy weighted average over the area of the GB unit cell is performed to obtain a mean embrittlement $\langle \Delta E_b^A \rangle$; this accounts for the coupling between occupancy and embrittlement and results in a mean contribution of solute segregation to embrittlement of the GB.

A. FS weighting

To compute an average over the ensemble of the FS permutations for a particular GB site, weights must be determined for the embrittling potency associated with each FS. It is likely that FS topographies with lower energy form more frequently during intergranular fracture. Thus, we assume that the weight for a particular embrittling potency depends on the relaxed energy of the corresponding FS. We do not consider dissipative events that lead to small structural rearrangements, such as dislocation nucleation from a crack tip, nor do we consider the effects of lattice trapping.

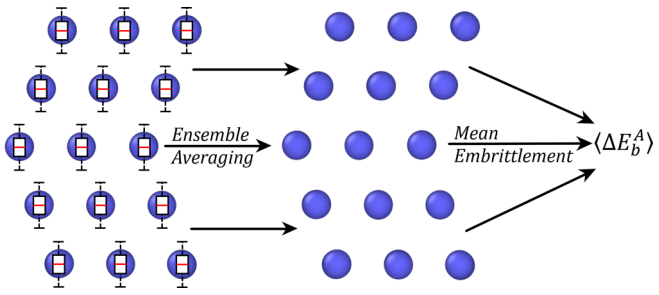

FIG. 6. The process of creating the mean embrittlement. Each site at the grain boundary (GB) begins with a distribution of embrittling potencies (left). Following an ensemble averaging procedure over many free surfaces, each site contains a single ensemble averaged embrittling potency (middle). Then an average is performed over all sites considering solute occupancy to obtain a mean embrittlement.

To obtain weights for embrittling potencies associated with FS energies, we require a tunable, monotonically decreasing distribution function. We expect that FSs are less likely to form if they have higher energies [46]. Hence, a survival function derived from Weibull fracture statistics serves our needs. Weibull-style functions are frequently used to describe distributions in studies of material strength and fracture [47–50], and its tunable size and shape parameters allow us to investigate the influence of including higher-energy FSs in the ensemble average for embrittlement.

We choose deliberately not to use the Boltzmann distribution, commonly used in statistical mechanics. While the NVT ensemble for which the Boltzmann distribution was derived has broad application, one of its core assumptions is that no work is or has been done on the system [51]. In our simulations, fracture is implied to occur between the GB and FS states, so work is considered to have been done on the system. Hence, the Boltzmann distribution is inappropriate for our approach.

Weibull fracture statistics, however, provide an appropriate lens through which we can examine our problem. In fracture statistics, elements of a material are envisioned as a series of nested chains and bundles, spanning in resolution from the continuum to the angstrom scale [52]. Failure of any one of these elements results in the failure of the entire structure, and failure is driven by an interplay between stress and the random distributions of kinetic energy among atoms, modeled by the Maxwell-Boltzmann distribution. One may consider the structures presented in this paper as being composed of such a lattice of chain and bundle elements, and the failure of the entire structure is envisioned as crack initiation. From empirical observations, we expect the GB unit elements to be the dominant volumes of failure, so a model that accounts for the failure of all such elements in the structure could be statistically approximated by a model which only observes failure at the GB elements. Thus, we view the weakest-link model as an appropriate statistical mechanics method for modeling intergranular fracture on the nanoscale.

From Bažant and Pang [52], if we assume that the stress is uniform, we may represent the probability of failure as a

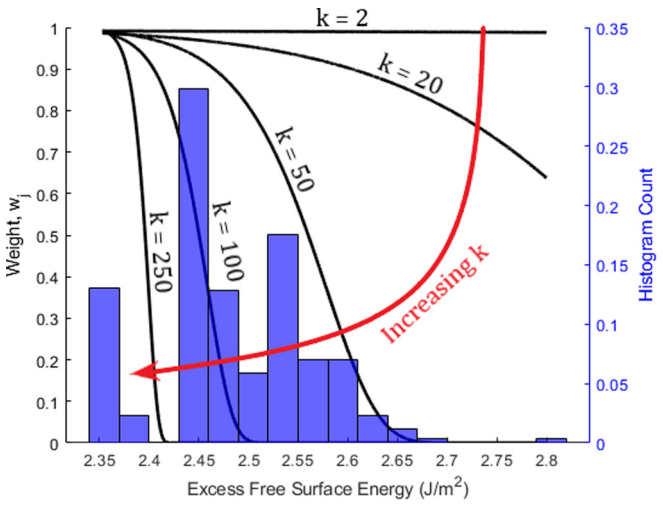

FIG. 7. Examples of Weibull survival functions with different k values for the $\Sigma 7$ {213} symmetric tilt grain boundary (STGB). The red arrow indicates increasing k. Higher k values result in lower weights for higher energy free surfaces.

cumulative distribution function $P_f(\sigma;\lambda,k)$, where σ is the stress acting on the volume, and λ and k are fitting parameters. The survival function is simply $1-P_f(\sigma;\lambda,k)$. While the survival function presented by Bažant and Pang [52] uses stress, thermodynamically, the fracture stress is proportional to the energy required to create two FSs from the GB model, i.e., $\sigma_f \propto 2E_j^{\mathrm{FS}} - E^{\mathrm{GB}}$. Recall from Fig. 5 that E_j^{FS} is the average FS energy for both surfaces. Since the energy of the GB is a constant for each model, we can simplify the previous statement to $\sigma_f \propto E_j^{\mathrm{FS}}$. Now the survival function provides a monotonically decreasing probability of survival based on FS energies and may be used as a weighting function for this paper. Since a Weibull distribution is best suited for weakest-link models [52], we write the weighting function as

$$w_j\left(E_j^{\mathrm{FS}};\lambda,k\right) = \exp\left[-\left(\frac{E_j^{\mathrm{FS}}}{\lambda}\right)^k\right]. \tag{5}$$

In this section, we choose a range of k values to compare, which physically represents different sets of FS permutations, and for each k fit a corresponding λ such that $w_j = 0.99$ at the minimum energy FS. This fitting is performed for each GB independently.

As an example, survival functions for the $\Sigma 7$ {213} STGB are shown in Fig. 7 overlayed on the histogram of the relaxed FS energies. Lower k values represent ensembles that include higher-energy FSs.

Utilizing different values of k allows us to answer the question: To what extent does inclusion of nonminimum energy FSs change the average embrittling behavior? As $k \to +\infty$, the survival function will approach the form of a step function, removing all FS data except that of the FS with the lowest formation energy. Likewise, as $k \to 1$, the survival function includes all FS data from higher-energy FSs into the ensemble. In other words, lower values of k represent a larger ensemble, i.e., more possible FS topographies, while larger values of k represent more limited ensembles, i.e., only lower-energy FS topographies. While $k \to +\infty$ represents the idealized circumstance of equilibrium fracture, we expect from atomistic simulations [24,27] that higher-energy FSs may appear during intergranular crack propagation, requiring these data to be included in the analysis of solute embrittlement.

For the proceeding discussion, we assume $k = 250$. We explore how this might affect our results by considering the following question: What is the FS energy range included by a particular value of k? For example, for $k = 250$, w_j is 0.05 at $E_j^{\mathrm{FS}} = 2.41$ J/m^2, so the included FS energy range is only [2.35, 2.41] J/m^2 or 0.06 J/m^2. For the $\Sigma 7$ {213} STGB, the area of a unit cell is ~69.7 Å^2, so the energy range for different FS topographies over the unit cell is 4.18×10^{-20} J or 0.26 eV. Lower k expand the FS energy range, while higher k shrink this range. This brief example provides some insight into the energetics associated with different intergranular fracture surfaces that may form under thermal and mechanical loading.

B. Ensemble averaged embrittling potency

With the FS weight w_j clearly defined, we now define an embrittling potency for each site $\langle \Delta E_{b,i} \rangle$ as a weighted average over the ensemble of many FS permutations j. Initially, this is done regardless of the segregation or antisegregation nature of the GB site. In this paper, we refer to this term as the *ensemble average embrittling potency*:

$$\langle \Delta E_{b,i} \rangle = \frac{1}{\sum_j w_j} \sum_j \Delta E_{b,ij} w_j. \tag{6}$$

Here, $\Delta E_{b,ij}$ is the embrittling potency of GB site i with FS topography j. The weight w_j is the probability of formation for FS topography j from Eq. (5). This provides each site with an embrittling potency that considers all sampled FS topographies and their likelihoods of appearing during fracture. This approach allows for the identification of critical sites for embrittlement. Values of $\langle \Delta E_{b,i} \rangle$ are shown for the $\Sigma 7$ {213} and the $\Sigma 21$ {415} STGBs in Figs. 8(a) and 8(b). Note that the ensemble average embrittling potency shows strengthening at the GB plane, indicating a reduced energetic preferences for Cr to be at the FS, which corroborates first-principles calculations by Startt *et al.* [29,30].

Recall, in the periodic GB ensemble, we repeat the FS topography decisions for each unit cell in the model, assuming that the topography adjacent to the segregation region is unimportant. To evaluate the impact of that assumption, we construct the flat neighboring ensemble, where the tortuous segregation region lies between flat neighboring cleavage planes above (or below) the GB, as discussed in Sec. II C. Figures 8(c) and 8(d) show results for the flat neighboring ensemble. Lastly, Figs. 8(e) and 8(f) show a comparative plot which takes the difference between the flat crack ensemble and original ensemble results. The greatest difference in magnitude is at the GB plane or the plane of atoms adjacent to the GB plane. Notably, the differences are mostly negative, suggesting that the flat neighboring ensemble shows more strengthening behavior. Differences for some sites were as large as −0.2 eV. Ultimately, evaluation of this additional ensemble provides an error estimation for the embrittling

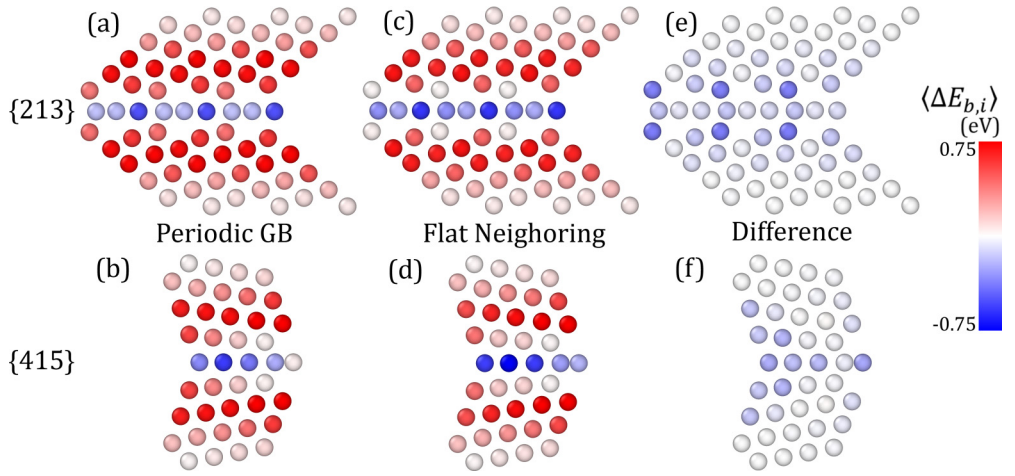

FIG. 8. The ensemble average embrittling potency $\langle \Delta E_{b,i} \rangle$ in electronvolts for each site i in the (a) Σ7 {213} symmetric tilt grain boundary (STGB) and the (b) Σ21 {415} STGB for the periodic grain boundary (GB) ensemble. Sites at the GB plane have a negative $\langle \Delta E_{b,i} \rangle$ (strengthening), while all other sites surrounding the GB layer have a positive $\langle \Delta E_{b,i} \rangle$ (embrittling). In these examples, $k = 250$ for the purpose of weighting site embrittling potencies. Flat neighboring ensemble for (c) Σ7 {213} and (d) Σ21 {415} STGBs. (e) and (f) Difference between the flat neighboring and periodic GB ensembles for each site.

potencies. This may warrant future studies devoted to understanding the impact of distant fracture surface topography on segregation energies and embrittling potencies.

It is important to understand the impact of different ensembles of FS topographies (represented by different values of k) on the ensemble average embrittling potency. Figure 9 shows that, as the size of the ensemble changes to include higher-energy FSs, the average site behavior can vary dramatically. In Fig. 9, the size of the ensemble is computed as the sum of FS weights $\sum w_j$, providing an effective number of FSs. Note the prediction for sites 2, 5, and 8 in the Σ7 {213} STGB and site 5 in the Σ21 {415} STGB can be either embrittling or strengthening depending on the number of FSs included in the ensemble. As $k \to +\infty$ and the ensemble reduces to only the minimum energy FS, we obtain the embrittling potency that would be reported in traditional segregation studies which rely only on the assumption of a single FS. However, including higher-energy FSs in the ensemble, represented by lower k values, shows a broader spectrum of embrittling behavior. In general, how the weighted averages change based on the size of the ensemble is unique to each site type, but it is clear from Fig. 9 that the inclusion of data from nonminimum energy FSs is important to the evaluation of embrittlement behavior. Note the choice $k = 250$ corresponds to 73 effective FSs considered for the Σ7 {213} STGB and 6 effective FSs considered for the Σ21 {415} STGB.

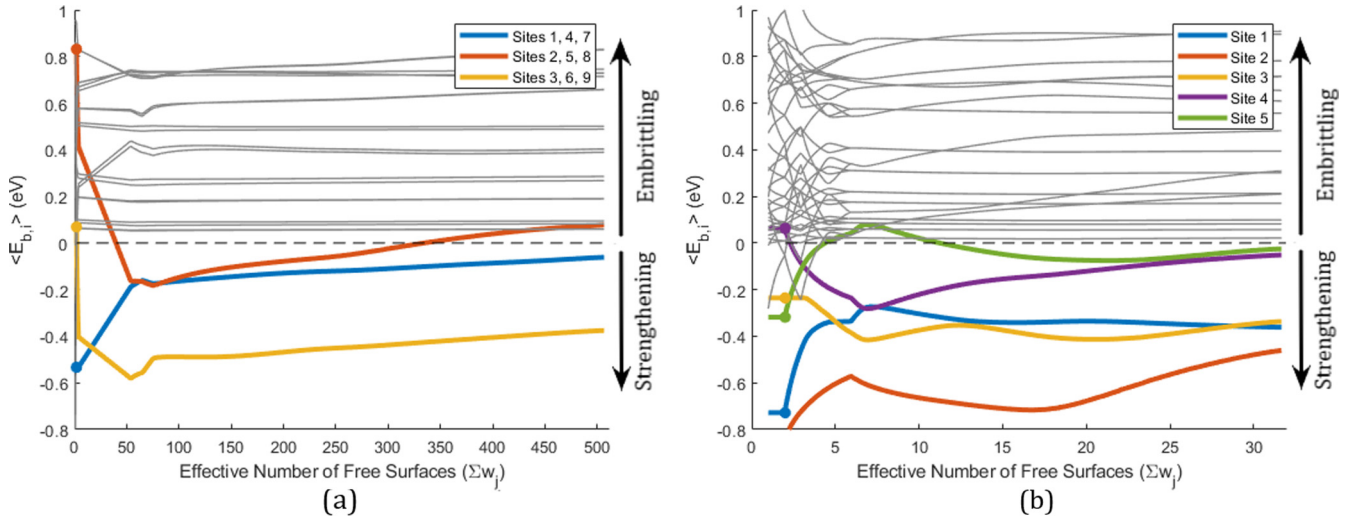

FIG. 9. Ensemble average embrittling potencies for (a) sites 1–9 in the Σ7 {213} symmetric tilt grain boundary (STGB) and (b) sites 1–5 in the Σ21 {415} STGB calculated via Eq. (6) plotted against effective number of free surface topographies. Note that, for $k = 250$, the Σ7 {213} STGB has 73 effective surfaces, while the Σ21 {415} STGB has 6. Gray lines mark the trajectories of sites off the grain boundary (GB), which are generally embrittling, as corroborated by Fig. 8.

C. Site occupancy probability

To average the $\langle \Delta E_{b,i} \rangle$ into a singular term for each GB, we need to consider occupancy probability for each GB site. Though the at. % occupancy X_i^{GB} provides insight into what sites are occupied, it does not represent the overall probability of a site being occupied. We can compute the site occupancy probability P_i^{GB} as

$$P_i^{\mathrm{GB}} = F_i^{\mathrm{GB}} X_i^{\mathrm{GB}}. \tag{7}$$

The density of states for interface sites F_i^{GB} can be computed if the number of interface sites of type i, denoted N_i^{GB}, is known. Interface site types are distinguished only by their segregation energy $\Delta E_{\mathrm{seg},i}^{\mathrm{GB}}$ [21]; thus,

$$F_i^{\mathrm{GB}} = \frac{N_i^{\mathrm{GB}}}{\sum N_i^{\mathrm{GB}}}. \tag{8}$$

Usually, site occupancy is computed for a wide variety of GBs to emulate a polycrystal [15,16,21]. When using many GB sites, the density of states becomes a nearly continuous function of the segregation energy. However, when considering only two GBs in isolation, as is done in this paper, we must treat the density of states discretely. To account for this, we simply consider the density of states as a constant value $F_i = \frac{1}{N}$, where N is the number of unique GB sites analyzed. The width of the GB, and hence N, is defined quantitatively using the segregation energy-based criterion detailed in Sec. III A. This is advantageous over a CNA approach [53], as CNA does not reveal all sites which impact the properties of the GB.

Importantly, note that Eq. (7) provides $X_i^{\mathrm{GB}} \cong P_i^{\mathrm{GB}} \cong 0$ for sites where $\Delta E_{i,\mathrm{seg}}^{\mathrm{GB}} \geqslant 0$, i.e., the probability of an antisegregation site being occupied is zero. Hence, when mean GB embrittlement is determined in Sec. IV D, antisegregation sites do not contribute to the mean, regardless of the value of $\langle \Delta E_{b,i} \rangle$.

D. Mean GB embrittlement

The ensemble average embrittling potency $\langle \Delta E_{b,i} \rangle$ provides a weighted average embrittling potency for each GB site. To develop a metric that describes the embrittling condition of the whole GB, we perform a sum weighted by site occupancy and normalized by the area of the unit cell A_{GB}:

$$\langle \Delta E_b^A \rangle = \frac{\sum_i \langle \Delta E_{b,i} \rangle P_i^{\mathrm{GB}}}{A_{\mathrm{GB}}}. \tag{9}$$

Here, the A superscript indicates normalization by area. $\langle \Delta E_b^A \rangle$ has units of energy per unit area and accounts for FS energetics, site occupancy, and structural properties of the GB. In this paper, we refer to this term as the *mean GB embrittlement*. The inspiration for this term comes from the Rice-Wang equation [13], which considers coverage as the number of solutes per unit area. To explain the development of Eq. (9), consider other possible formulations of $\langle \Delta E_b \rangle$. One formulation considered was a weighted sum normalized by the site occupancy:

$$\langle \Delta E_b^P \rangle = \frac{\sum_i \langle \Delta E_{b,i} \rangle P_i^{\mathrm{GB}}}{\sum_i P_i^{\mathrm{GB}}}. \tag{10}$$

Here, the P superscript indicates normalization by the site occupancy. In this approach, the mean GB embrittlement has units of energy. To assess Eq. (10), consider a hypothetical GB with a single unique site type. Suppose we have two different alloying cases, such that case 1 has a low P_i^{GB} and positive, high magnitude $\langle \Delta E_{b,i} \rangle$, and case 2 has a high P_i^{GB} and positive, low magnitude $\langle \Delta E_{b,i} \rangle$. For the sake of this example, suppose that $\langle \Delta E_b^A \rangle^{(1)} = \langle \Delta E_b^A \rangle^{(2)}$, or otherwise stated, $\sum_i \langle \Delta E_{b,i} \rangle^{(1)} P_i^{\mathrm{GB}(1)} = \sum_i \langle \Delta E_{b,i} \rangle^{(2)} P_i^{\mathrm{GB}(2)}$ with $i = 1$. Equation (9) suggests that these two cases result in identical embrittlement of the GB, which agrees with the Rice-Wang equation [13]. However, since $P_i^{\mathrm{GB}(1)} < P_i^{\mathrm{GB}(2)}$, normalizing by the sum of P_i^{GB} as in Eq. (10) would result in case 1 being more embrittling than case 2. While it is true that case 1 has a higher embrittling potency for its site, case 2 overcomes the lower embrittling potency with higher occupancy. Hence, energetically, these two cases should be represented identically if a metric is to be used as a comparative term between GBs, and clearly, Eq. (10) cannot be used for this purpose.

To justify the area normalization in Eq. (9), consider the weighted sum with no normalization:

$$\langle \Delta E_b \rangle = \sum_i \langle \Delta E_{b,i} \rangle P_i^{\mathrm{GB}}. \tag{11}$$

To test Eq. (11), consider an example with two GBs which differ in size and structure. In this case, assume that $\sum \langle E_{b,i}^{(1)} \rangle P_i^{\mathrm{GB}(1)} < \sum \langle E_{b,i}^{(2)} \rangle P_i^{\mathrm{GB}(2)}$, $A_{\mathrm{GB}}^{(1)} < A_{\mathrm{GB}}^{(2)}$, and $\frac{\sum \langle E_{b,i}^{(1)} \rangle P_i^{\mathrm{GB}(1)}}{A_{\mathrm{GB}}^{(1)}} = \frac{\sum \langle E_{b,i}^{(2)} \rangle P_i^{\mathrm{GB}(2)}}{A_{\mathrm{GB}}^{(2)}}$. Since the embrittlement effect in the Rice-Wang equation [13] requires both embrittling potency and segregant coverage per unit area, we expect both cases to be equally embrittling over the same area. However, if we compare these GBs using Eq. (11), then case 2 would be more embrittling than case 1, which contradicts the motivation the Rice-Wang equation [13] provides.

According to these hypothetical examples that consider both chemically and geometrically variate cases, if the objective is for $\langle \Delta E_b \rangle$ to be a term that characterizes the effect of a solute on a particular GB and provides fair comparison between two GBs, then it is necessary to use Eq. (9) with area normalization. While Eq. (10) more closely resembles the original definition of embrittling potency (as a term with units of energy), the normalization deleteriously changes the way occupancy impacts the average. Similarly, Eq. (11) provides a sum of the embrittling potencies over a GB unit cell, but GBs with larger unit cells would appear to have larger embrittlement magnitude when compared against GBs with smaller unit cells if not area normalized.

Thus, using the segregation and FS energies generated by atomistic calculations in this paper, we find that $\langle \Delta E_b \rangle = 1.018 \times 10^{-3}$ eV/Å^2 for the $\Sigma 7$ {213} STGB and $\langle \Delta E_b \rangle = 1.482 \times 10^{-3}$ eV/Å^2 for the $\Sigma 21$ {415} STGB. Thus, the $\Sigma 21$ {415} STGB is predicted to be 45.7% more embrittled by the presence of Cr solutes than the $\Sigma 7$ {213} STGB when averaged over the ensemble of many FSs and considering differences in GB area.

Recall from Fig. 5 that the black dots represent the embrittling potency of sites considering only the lowest-energy FS pair, where $k \to +\infty$. Previous studies have only considered

this data point and have ignored the influence of the intergranular fracture surface topography. Suppose we calculate a mean GB embrittlement using only values for the minimum energy FS for the Σ7 {213} STGB. This results in $\Delta E_b^A = 1.778 \times 10^{-3}$ eV/Å^2. This value overpredicts the $k = 250$ ensemble average value of $\langle \Delta E_b^A \rangle = 1.018 \times 10^{-3}$ eV/Å^2 by 75%. Similarly, if we calculated the mean GB embrittlement for the Σ21 {415} STGB using only the minimum energy FS, this results in $\Delta E_b^A = 1.878 \times 10^{-3}$ eV/Å^2, which overshoots the $k = 250$ ensemble average value by 27%. Although it still predicts the same relative relationship, that the Σ21 {415} STGB is more embrittled by Cr solutes than the Σ7 {213} STGB, using the minimum energy fracture surface only predicts a less significant discrepancy of 5.6%, whereas the discrepancy is 45.7% in the ensemble case for the selected value of k. Note that the relative difference is not preserved for different k and may change depending on the ensemble.

These results highlight the significance of considering a statistical perspective when studying solute-induced intergranular embrittlement. The value for k here is selected as an example considering the FS energy range, but for any ensemble where $k \neq \infty$, as shown in Fig. 9, there will be a difference between the embrittlement for the minimum energy FS and the embrittlement for an ensemble of FSs. This ensemble perspective is more inclusive of different intergranular fracture surface topographies that are observed during experiments and atomistic simulations.

V. CONCLUSIONS

In this paper, we propose a statistical perspective on solute-induced GB embrittlement by considering an ensemble of FSs in the analysis. Specifically, atomistic simulations of Cr segregation at Ni Σ7 {213} and Σ21 {415} ⟨111⟩ STGBs are performed to compute distributions of embrittling potencies for each GB site generated by sampling different FS topographies. Statistical mechanics principles are used to condense the resulting distributions of embrittling potencies into a singular value for each GB site, called the ensemble average embrittling potency. These embrittling potencies are then weighted by the site occupancy and averaged over the unit cell area to provide a measure of mean GB embrittlement. Ultimately, the ensemble perspective provides a new term to compare the embrittling effects of solutes between different GBs [Eq. (9)], which is then used to assess the average embrittlement effect of Cr segregation at Ni Σ7 {213} and Σ21 {415} ⟨111⟩ STGBs. All calculations are performed within the dilute limit, ignoring solute-solute interactions.

Previously, studies of embrittling potencies have generally ignored the impact of FS topography formed during fracture and have treated embrittling potency as a singular value for a selected GB. In this paper, we demonstrate that an ensemble of FSs is necessary to completely understand embrittlement; there is a spectrum of embrittlement behavior exhibited by each GB site. The distributions of embrittling potency demonstrate cases where a site can be either strengthening or weakening depending on the FS topography. In addition, the magnitude of the embrittlement or strengthening effect of a solute depends on the FS considered.

ACKNOWLEDGMENTS

M.F. and D.E.S. acknowledge support provided by Sandia National Laboratories and the University of Florida. R.D. is supported by the U.S. Department of Energy (DOE) Office of Basic Energy Sciences, Department of Materials Science and Engineering. The authors acknowledge University of Florida Research Computing for providing computational resources and support that have contributed to the research results reported in this publication. The authors thank Dr. C. Hu for providing useful comments on a draft of this manuscript. The work in this paper was performed, in part, at the Center for Integrated Nanotechnologies, an Office of Science User Facility operated for the U.S. DOE. Sandia National Laboratories is a multimission laboratory managed and operated by National Technology and Engineering Solutions of Sandia, LLC, a wholly owned subsidiary of Honeywell International, Inc., for the U.S. DOE's National Nuclear Security Administration under Contract No. DE-NA0003525. This paper describes objective technical results and analysis. Any subjective views or opinions that might be expressed in the paper do not necessarily represent the views of the U.S. DOE or the United States Government.

[1] E. Martínez, B. P. Uberuaga, and B. D. Wirth, Atomistic modeling of helium segregation to grain boundaries in tungsten and its effect on de-cohesion, Nucl. Fusion. **57**, 086044 (2017).

[2] M. C. Inman and H. R. Tipler, Grain-Boundary segregation of phosphorus in an iron-phosphorus alloy and the effect upon mechanical properties, Acta Metall. **6**, 73 (1958).

[3] S. L. Cundy, A. J. F. Metherell, M. J. Whelan, P. N. T. Unwin, and R. B. Nicholson, Studies of segregation and the initial stages of precipitation at grain boundaries in an aluminium 7 wt. % magnesium alloy with an energy analysing electron microscope, Proc. R. Soc. Lond. A **307**, 267 (1968).

[4] D. E. Spearot, G. J. Tucker, A. Gupta, and G. B. Thompson, Mechanical properties of stabilized nanocrystalline FCC metals, J. Appl. Phys. **126**, 110901 (2019).

[5] D. N. F. Muche, A. L. da Silva, K. Nakajima, D. Gouvêa, and R. H. R. Castro, Simultaneous segregation of lanthanum to surfaces and grain boundaries in $MgAl_2O_4$ nanocrystals, Appl. Surf. Sci. **529**, 147145 (2020).

[6] J. M. Monti, E. M. Hopkins, K. Hattar, F. Abdeljawad, B. L. Boyce, and R. Dingreville, Stability of immiscible nanocrystalline alloys in compositional and thermal fields, Acta Mater. **226**, 117620 (2022).

[7] W. T. Geng, A. J. Freeman, and G. B. Olson, Influence of alloying additions on grain boundary cohesion of transition metals: first-principles determination and its phenomenological extension, Phys. Rev. B **63**, 165415 (2001).

[8] W. Barrows, R. Dingreville, and D. Spearot, Traction-separation relationships for hydrogen induced grain boundary embrittle-

ment in nickel via molecular dynamics simulations, Mater. Sci. Eng. A **650**, 354 (2016).

[9] P. Gupta, K. K. Chattopadhyay, S. Chaudhuri, and A. K. Pal, II–VI semiconductor alloy films: $Cd_{1-x}Zn_xTe$, J. Mater. Sci. **28**, 496 (1993).

[10] H.-I. Hsiang and J.-L. Wu, Copper-rich phase segregation effects on the magnetic properties and DC-bias-superposition characteristic of NiCuZn ferrites, J. Magn. Magn. Mater. **374**, 367 (2015).

[11] T. G. Langdon, Significance of grain boundaries in the flow of polycrystalline materials, Mater. Sci. Forum **189–190**, 31 (1995).

[12] M. A. Shtremel and O. V. Zhevnerova, Stochastic geometry of the surface of grain-boundary fracture, Phys. Met. Metallogr. **91**, 94 (2000).

[13] J. R. Rice and J. S. Wang, Embrittlement of interfaces by solute segregation, Mater. Sci. Eng. A **107**, 23 (1989).

[14] D. McLean, *Grain Boundaries in Metals* (Oxford University Press, New York, 1957).

[15] C. L. White and D. F. Stein, Sulfur segregation to grain boundaries in Ni_3Al and $Ni_3(AI, Ti)$ alloys, Metall. Trans. A **9**, 13 (1978).

[16] C. L. White and W. A. Coghlan, The spectrum of binding energies approach to grain boundary segregation, Metall. Trans. A **8**, 1403 (1977).

[17] X. Wu, Y.-W. You, X.-S. Kong, J.-L. Chen, G.-N. Luo, G.-H. Lu, C. S. Liu, and Z. Wang, First-principles determination of grain boundary strengthening in tungsten: dependence on grain boundary structure and metallic radius of solute, Acta Mater. **120**, 315 (2016).

[18] X. Xing, G. Deng, H. Zhang, G. Cui, J. Liu, Z. Li, B. Wang, S. Li, and C. Qi, Molecular dynamics studies of hydrogen effect on intergranular fracture in α-iron, Materials **13**, 4949 (2020).

[19] M. Yamaguchi, M. Shiga, and H. Kaburaki, First-principles study on segregation energy and embrittling potency of hydrogen in NiΣ5(012) tilt grain boundary, J. Phys. Soc. Jpn. **73**, 441 (2004).

[20] V. I. Razumovskiy, A. Y. Lozovoi, and I. M. Razumovskii, First-principles-aided design of a new Ni-base superalloy: influence of transition metal alloying elements on grain boundary and bulk cohesion, Acta Mater. **82**, 369 (2015).

[21] D. Aksoy, R. Dingreville, and D. E. Spearot, Spectrum of embrittling potencies and relation to properties of symmetric-tilt grain boundaries, Acta Mater. **205**, 116527 (2021).

[22] V. I. Razumovskiy, D. Scheiber, I. M. Razumovskii, V. N. Butrim, A. S. Trushnikova, S. B. Varlamova, and A. G. Beresnev, New Cr-Ni-base alloy for high-temperature applications designed on the basis of first principles calculations, Adv. Condens. Matter Phys. **2018**, 9383981 (2018).

[23] A. Latapie and D. Farkas, Molecular dynamics investigation of the fracture behavior of nanocrystalline α-Fe, Phys. Rev. B **69**, 134110 (2004).

[24] D. E. Spearot, K. I. Jacob, and D. L. McDowell, Non-local separation constitutive laws for interfaces and their relation to nanoscale simulations, Mech. Mater. **36**, 825 (2004).

[25] M. Seita, J. P. Hanson, S. Gradečak, and M. J. Demkowicz, The dual role of coherent twin boundaries in hydrogen embrittlement, Nat. Commun. **6**, 6164 (2015).

[26] V. Yamakov, E. Saether, D. R. Phillips, and E. H. Glaessgen, Dynamic Instability in Intergranular Fracture, Phys. Rev. Lett. **95**, 015502 (2005).

[27] E. Bitzek, J. R. Kermode, and P. Gumbsch, Atomistic aspects of fracture, Int. J. Fract. **191**, 13 (2015).

[28] A. Tehranchi and W. A. Curtin, Atomistic study of hydrogen embrittlement of grain boundaries in nickel: I. Fracture, J. Mech. Phys. Solids **101**, 150 (2017).

[29] J. Startt, R. Dingreville, S. Raiman, and C. Deo, An electronic origin to the oscillatory segregation behavior in Ni-Cr and other BCC defects in FCC metals, Acta Mater. **218**, 117215 (2021).

[30] J. Startt, C. Deo, and R. Dingreville, Vacancy surface migration mechanisms in dilute nickel-chromium alloys, Scr. Mater. **202**, 113998 (2021).

[31] S. Plimpton, Fast parallel algorithms for short-range molecular dynamics, J. Comput. Phys. **117**, 1 (1995).

[32] A. P. Thompson, H. M. Aktulga, R. Berger, D. S. Bolintineanu, W. M. Brown, P. S. Crozier, P. J. Veld, A. Kohlmeyer, S. G. Moore, T. D. Nguyen *et al.*, LAMMPS—a flexible simulation tool for particle-based materials modeling at the atomic, meso, and continuum scales, Comput. Phys. Commun. **271**, 108171 (2022).

[33] X. W. Zhou, M. E. Foster, and R. B. Sills, An Fe-Ni-Cr embedded atom method potential for austenitic and ferritic systems, J. Comput. Chem. **39**, 2420 (2018).

[34] C. Wu, B.-J. Lee, and X. Su, Modified embedded-atom interatomic potential for Fe-Ni, Cr-Ni and Fe-Cr-Ni systems, Calphad **57**, 98 (2017).

[35] C. A. Howells and Y. Mishin, Angular-dependent interatomic potential for the binary Ni-Cr system, Model. Simul. Mater. Sci. Eng. **26**, 085008 (2018).

[36] A. Stukowski, Visualization and analysis of atomistic simulation data with OVITO—the open visualization tool, Model. Simul. Mater. Sci. Eng. **18**, 015012 (2010).

[37] C. L. Kelchner, S. J. Plimpton, and J. C. Hamilton, Dislocation nucleation and defect structure during surface indentation, Phys. Rev. B **58**, 11085 (1998).

[38] R. Dingreville, D. Aksoy, and D. E. Spearot, A primer on selecting grain boundary sets for comparison of interfacial fracture properties in molecular dynamics simulations, Sci. Rep. **7**, 8332 (2017).

[39] Gui Jin Wang, A. P. Sutton, and V. Vitek, A computer simulation study of $\langle 001 \rangle$ and $\langle 111 \rangle$ tilt boundaries: the multiplicity of structures, Acta Metall. **32**, 1093 (1984).

[40] M. Wagih and C. A. Schuh, Grain boundary segregation beyond the dilute limit: separating the two contributions of site spectrality and solute interactions, Acta Mater. **199**, 63 (2020).

[41] M. I. Mendelev, M. Asta, M. J. Rahman, and J. J. Hoyt, Development of interatomic potentials appropriate for simulation of solid-liquid interface properties in Al-Mg alloys, Philos. Mag. **89**, 3269 (2009).

[42] C. Hu, Y. Li, Z. Yu, and J. Luo, Computing grain boundary diagrams of thermodynamic and mechanical properties, Npj Comput. Mater. **7**, 159 (2021).

[43] J. Luo, H. Cheng, K. M. Asl, C. J. Kiely, and M. P. Harmer, The role of a bilayer interfacial phase on liquid metal embrittlement, Science **333**, 1730 (2011).

[44] M. Wagih and C. A. Schuh, Spectrum of grain boundary segregation energies in a polycrystal, Acta Mater. **181**, 228 (2019).

[45] D. Freedman and P. Diaconis, On the histogram as a density estimator: L2 theory, Z. Wahrscheinlichkeitstheorie Verwandte Geb. **57**, 453 (1981).

[46] V. Ryabov, *Principles of Statistical Physics and Numerical Modeling* (IOP Publishing, Bristol, 2018).

[47] B. Basu, D. Tiwari, D. Kundu, and R. Prasad, Is Weibull distribution the most appropriate statistical strength distribution for brittle materials? Ceram. Int. **35**, 237 (2009).

[48] D. Djeghader and B. Redjel, Effect of water absorption on the Weibull distribution of fatigue test in jute-reinforced polyester composite materials, Adv. Compos. Lett. **28**, 1 (2019).

[49] M. Alqam, R. M. Bennett, and A.-H. Zureick, Three-parameter vs. two-parameter Weibull distribution for pultruded composite material properties, Compos. Struct. **58**, 497 (2002).

[50] S. Nadarajah and S. Kotz, Strength modeling using Weibull distributions, J. Mech. Sci. Technol. **22**, 1247 (2008).

[51] X. Gao, E. Gallicchio, and A. E. Roitberg, The generalized Boltzmann distribution is the only distribution in which the Gibbs-Shannon entropy equals the thermodynamic entropy, J. Chem. Phys. **151**, 034113 (2019).

[52] Z. P. Bažant and S. D. Pang, Activation energy based extreme value statistics and size effect in brittle and quasibrittle fracture, J. Mech. Phys. Solids **55**, 91 (2007).

[53] Z. Pan and T. J. Rupert, Formation of ordered and disordered interfacial films in immiscible metal alloys, Scr. Mater. **130**, 91 (2017).